Available online at www.sciencedirect.com
SCIENCE DIRECT®
Journal of Magnetic Resonance xxx (2006) xxx–xxx
JMR Journal of Magnetic Resonance
www.elsevier.com/locate/jmr

Efficient simulation of magnetic resonance imaging with Bloch–Torrey equations using intra-voxel magnetization gradients

Thies H. Jochimsen [a,*], Andreas Schäfer [b], Roland Bammer [a], Michael E. Moseley [a]

[a] *Lucas MRS/I Center, Department of Radiology, Stanford University, 1201 Welch Road, Stanford, CA 94305, USA*
[b] *Max Planck Institute for Human Cognitive and Brain Sciences, Stephanstr. 1a, D-04103 Leipzig, Germany*

Received 4 October 2005; revised 23 November 2005

Abstract

The process of image formation in magnetic resonance imaging (MRI) can be simulated by means of an iterative solution of Bloch–Torrey equations. This is a useful accessory to analyze the influence of sample properties, sequence parameters and hardware specifications on the MRI signal. In this paper, a computer algorithm is presented which is based on calculating partial derivatives of the magnetization vector. This technique allows more efficient simulation than summation of isochromats (the latter being commonly employed for this purpose) and, as a result, the effect of diffusion on the MRI signal can be calculated iteratively. A detailed description of the algorithm is given, and its feasibility for different applications is studied. It is shown that the algorithm is most applicable to simulating the effect of field perturbations, i.e. intra-voxel dephasing, but is also useful for other typical imaging experiments and the simulation of diffusion weighting.

Keywords: Magnetic resonance imaging; Simulation; Bloch–Torrey equations; Intra-voxel dephasing; Field inhomogeneity; Diffusion

1. Introduction

As a supplement to magnetic resonance imaging (MRI) experiments, numerical simulation of MRI sequences based on solutions of Bloch–Torrey equations [1] provides additional insight into the process of image formation. There are numerous examples where simulation can be useful:

- Optimization of MR sequences without the need of costly measurements.
- Analyzing the effect of field perturbations [2].
- Investigating the effects of in-plane flow [3].
- Estimating inversion efficiency of in vivo arterial spin-labeling [4].
- Rapid prototyping of MRI sequences [5].

The first description of a simulator for MRI imaging was given by Bittoun et al. [1]. It uses the solutions of Bloch equations for one point and one frequency of the object (i.e., for one isochromat) and generates the global MRI signal by accumulating the signal from many isochromats of the object. Thereby, the isochromats differ by frequency offset due to different spatial offsets in the field gradients of the imaging sequence. This isochromat summation (ISUM) was adapted in a number of subsequent studies [2,3,6–11]. In general, the accuracy of the simulation increases with the number of isochromats and hence with simulation time (*ST*), which is the time required to complete the simulation. In particular, when using a too limited number of isochromats, the following problems arise:

- Simulation is performed only at discrete spatial locations. In order to mimic a continuous distribution of spins throughout the voxel, a considerable number of isochromats is required per imaging voxel to generate a smooth image intensity. If the number of isochromats

* Corresponding author. Fax: +1 650 723 5795.
E-mail address: thies@stanford.edu (T.H. Jochimsen).

1090-7807/$ - see front matter © 2006 Published by Elsevier Inc.
doi:10.1016/j.jmr.2006.01.001

is too low, spurious patterns appear in the simulated image. It was estimated that at least three isochromats per voxel and direction are necessary in order to reduce the error of image intensity to less than 1.5% [7].

- Even with a large number of evenly distributed isochromats per voxel, gradient spoiling can produce artificial maxima if the spoiling strength is chosen so that, accidentally, all isochromats differ only by a phase of 2π, i.e. they interfere constructively [3]. Distributing the isochromats randomly over the voxel might circumvent the generation of false maxima, but may introduce artificial fluctuations of image magnitude.
- In complex objects, such as biological tissue, a voxel contains a mixture of isochromats with different resonance frequencies. These may be, for example, due to local field gradients in inhomogeneous media or different chemical shifts. This distribution of frequencies leads to intra-voxel dephasing and rephasing after the application of radio-frequency (RF) pulses, i.e., to field-inhomogeneity-induced signal decay, spin echoes or stimulated echoes. In order to simulate these effects accurately, a large number of isochromats with different resonance frequencies is usually required per voxel [9].

To obtain N imaging voxels per spatial dimension using a number of input voxels with a fixed ratio relative to N, the number of computational steps is of the order of N^2. In two-dimensional imaging, this results in a fourth-order process ($ST \sim N^4$). By considering a distribution of isochromats in each voxel, the number of required steps is increased further. Thus, even with contemporary hardware or parallelized implementations [8], the simulation of complex sequences or objects may be impractical by ISUM. A technique to accelerate simulation is the use of tissue templates [9]. Unfortunately, this technique does not cover the simulation of field distortions. Another limitation of present-day simulation strategies is that they do not include the effect of molecular self-diffusion on the MRI signal in a general way.

The present work suggests an alternative approach to increase simulation efficiency and to simulate self-diffusion: in addition to tracing the evolution of magnetization at a certain position and frequency $(\boldsymbol{r},\omega)$, the evolution in the immediate vicinity of this point is also traced. This is done by calculating iteratively the intra-voxel magnetization gradients, i.e., the partial derivatives (PDs) of the magnetization vector, with respect to position and frequency. That is, a linearization is performed for a small region centered about the isochromat, i.e., the voxel, and the evolution of magnetization over a continuum of spatial positions and frequencies is traced simultaneously. This parameterization allows extrapolation of the magnetization vector to different locations and frequencies. This magnetization-gradient based simulation of intra-voxel dephasing (MAGSI) has two applications: First, it is possible to calculate the total MRI signal by phase-sensitive integrations over voxels and frequency intervals. Thus, the number of computational steps and hence ST, which is necessary for an accurate simulation, can be reduced significantly in comparison to ISUM. Second, the attenuation due to self-diffusion can be simulated iteratively.

2. Methods

2.1. Input to simulation

The simulation was implemented within the ODIN framework [5] using the C++ programming language. ODIN describes an MRI sequence in terms of sequence objects (RF pulses, gradient pulses, acquisition periods). Thereby, each sequence object occupies a number of channels (RF transmitter, gradients, and signal receiver) and defines a set of discrete time intervals. For example, an acquisition object will contribute a number of sampling points separated by the dwell time, and a shaped RF pulse will provide an array representing the complex waveform of the RF field. The set union of all time points enclosing the time intervals and proper interpolation of values on all channels then forms the piecewise-constant time course of the whole sequence. Each interval of this piecewise-constant array is then used for one iteration during simulation. This strategy ensures that time resolution is high when necessary (e.g., during shaped RF pulses, data acquisition) and low if unnecessary (e.g., timing/relaxation delays which can be covered by one long iteration).

In addition, a virtual sample is required which serves as input to the simulation by describing the properties of the object, namely relaxation constants T_1 and T_2, diffusion coefficient/tensor D, frequency offset ω and equilibrium magnetization M_0. Each property is a function of spatial position and frequency and can either be obtained by measurement or by numerical models. In the following, the term *isochromat* will be used to label a single point of this discretized data set. Alternatively, to emphasize the (finite) spatial extent of this data point, the term *input voxel* will also be employed. In contrast, *imaging voxel* denotes a single point of the reconstructed image. In addition, to provide a consistent treatment of the dependency of the magnetization vector upon spatial position and frequency, we will use the term *voxel* to describe not only a three-dimensional range of spatial positions (i.e., a volume element), but also a certain range of frequencies.

2.2. Bloch–Torrey equations

The starting point for our considerations is the evolution of an isochromat, i.e., of a magnetization vector, which is described by the Bloch–Torrey equations [12]

$$\dot{\boldsymbol{M}} = \boldsymbol{M} \times \boldsymbol{\Omega} - \begin{pmatrix} M_x/T_2 \\ M_y/T_2 \\ (M_z - M_0)/T_1 \end{pmatrix} + \begin{pmatrix} \nabla \cdot D\nabla M_x \\ \nabla \cdot D\nabla M_y \\ \nabla \cdot D\nabla M_z \end{pmatrix} \quad (1)$$

with the magnetization vector $\boldsymbol{M} = \boldsymbol{M}(\boldsymbol{r}, t) = (M_x, M_y, M_z)^\top$ in rotating reference frame, indexed in the following by (x, y, z). Here, $\boldsymbol{\nabla} = (\frac{\partial}{\partial r_1}, \frac{\partial}{\partial r_2}, \frac{\partial}{\partial r_3})^\top$ is applied in the laboratory reference frame spanned by (r_1, r_2, r_3), and $\mathbf{D}$ is the diffusion tensor ($\mathbf{D} = D\mathbb{I}$ in the case of isotropic diffusion with a constant D). Fields in addition to the main magnetic field are combined by

$$\boldsymbol{\Omega} = \boldsymbol{\Omega}(\boldsymbol{r}, t) = (\Omega_x, \Omega_y, \Omega_z)^\top = \left(\gamma B_1^{\mathrm{re}}(\boldsymbol{r}, t),\ \gamma B_1^{\mathrm{im}}(\boldsymbol{r}, t),\ \gamma \boldsymbol{G}(t)\boldsymbol{r} + \omega(\boldsymbol{r})\right)^\top. \quad (2)$$

Thereby, γ denotes the gyromagnetic ratio, $B_1 = B_1^{\mathrm{re}} + \mathrm{i}B_1^{\mathrm{im}}$ is the complex RF field, $\boldsymbol{G}$ the externally applied gradient-field vector, and ω accounts for the frequency offset of the isochromat observed.

2.3. Iterative solution of Bloch–Torrey equations for ISUM

A solution of Eq. (1) with piecewise constant fields (and omitting diffusion) is given in [13]. Based on this solution, the evolution of an isochromat can be calculated iteratively (as for example in [4]). We will extend this approach by an additional iterative step which takes into account unrestricted self diffusion. The iterative solution is simplified by two assumptions: First, if $\Delta t \ll T_1, T_2$ during periods with RF irradiation, where Δt is the duration of one iteration, irradiation and relaxation can be considered as two subsequent processes. Second, the so-called *hard-pulse approximation* is used, where shaped RF pulses are considered as sequences of hard pulses, i.e., pulses which rotate all isochromats the same amount, interleaved with periods of free precession [14]. With these simplifications, it is possible to express the iterative solution, i.e., the magnetization vector at the $i+1$ time step, by successive application of matrix operations:

$$\boldsymbol{M}_{i+1} = \mathrm{E}\mathrm{A}_D\mathrm{R}_{\mathrm{RF}}\mathrm{R}_z\boldsymbol{M}_i + \boldsymbol{E}_0 \quad (3)$$

with an initial condition $\boldsymbol{M}_0 = (0, 0, M_0)^\top$. Relaxation is accounted for by

$$\mathrm{E} = \mathrm{diag}(\mathrm{e}^{-\Delta t/T_2},\ \mathrm{e}^{-\Delta t/T_2},\ \mathrm{e}^{-\Delta t/T_1}) \quad \text{and} \quad \boldsymbol{E}_0 = (0, 0, M_0(1 - \mathrm{e}^{-\Delta t/T_1}))^\top. \quad (4)$$

Due to unrestricted self-diffusion, the magnetization vector is attenuated at each iteration by

$$\mathrm{A}_D = \mathrm{diag}(\mathrm{e}^{-\beta_2 D},\ \mathrm{e}^{-\beta_2 D},\ \mathrm{e}^{-\beta_1 D}) \quad (5)$$

with the (isotropic) diffusion coefficient D. In Appendix A, formulae will be presented to calculate the factors β_1 and β_2 using magnetization gradients. The rotation matrix due to the application of RF pulses is

$$\mathrm{R}_{\mathrm{RF}} = \begin{pmatrix} a_x^2 + a_y^2\cos\theta_{\mathrm{RF}} & a_x a_y(1-\cos\theta_{\mathrm{RF}}) & -a_y\sin\theta_{\mathrm{RF}} \\ a_x a_y(1-\cos\theta_{\mathrm{RF}}) & a_y^2 + a_x^2\cos\theta_{\mathrm{RF}} & a_x\sin\theta_{\mathrm{RF}} \\ a_y\sin\theta_{\mathrm{RF}} & -a_x\sin\theta_{\mathrm{RF}} & \cos\theta_{\mathrm{RF}} \end{pmatrix} \quad (6)$$

with $\Omega_1 = \gamma|B_1|$, $a_x = \dfrac{\Omega_x}{\Omega_1}$, $a_y = \dfrac{\Omega_y}{\Omega_1}$, and $\theta_{\mathrm{RF}} = \Omega_1\Delta t$. (7)

Finally, off-resonance effects due to local field inhomogeneity, chemical shift, or externally applied gradient fields are taken into account by the rotation matrix

$$\mathrm{R}_z = \begin{pmatrix} \cos\theta_z & \sin\theta_z & 0 \\ -\sin\theta_z & \cos\theta_z & 0 \\ 0 & 0 & 1 \end{pmatrix} \quad \text{with} \quad \theta_z = \Omega_z\Delta t. \quad (8)$$

2.4. Evolution of intra-voxel magnetization gradients for MAGSI

For the following, it is suggestive to think of $\boldsymbol{M}$ being a function of spatial position and frequency offset: $\boldsymbol{M} = \boldsymbol{M}(\boldsymbol{r}, \omega) = \boldsymbol{M}(r_1, r_2, r_3, \omega)$. In order to trace the evolution of intra-voxel magnetization gradients for MAGSI, partial derivatives of $\boldsymbol{M}$ with respect to $\boldsymbol{r}$ and ω of the iterative solution (Eq. (3)) will be calculated. To simplify notation in the following, k subscripts the three spatial dimensions and the frequency dimension: $k = \{r_1, r_2, r_3, \omega\}$, and the symbol ∂_k denotes the partial derivative in k'th direction at the center of the voxel, i.e., $\partial_k \ldots = \frac{\partial}{\partial k}\ldots|_{k=0}$. By assuming that B_1, M_0, T_2, T_1 and D do not vary throughout the voxel (i.e., $\partial_k B_1 = \partial_k M_0 = \partial_k T_2 = \partial_k T_1 = \partial_k D = 0$), it follows that $\partial_k \mathrm{R}_{\mathrm{RF}} = \partial_k \mathrm{E} = \partial_k \boldsymbol{E}_0 = \partial_k \mathrm{A}_D = 0$. By applying partial derivation to Eq. (3) and using the product rule of derivation (which also applies to matrix multiplication), one obtains

$$\partial_k\boldsymbol{M}_{i+1} = \mathrm{E}\mathrm{A}_D\mathrm{R}_{\mathrm{RF}}\partial_k[\mathrm{R}_z\boldsymbol{M}_i] = \mathrm{E}\mathrm{A}_D\mathrm{R}_{\mathrm{RF}}[(\partial_k\mathrm{R}_z)\boldsymbol{M}_i + \mathrm{R}_z\partial_k\boldsymbol{M}_i] \quad (9)$$

with

$$\partial_k\mathrm{R}_z = h_k\begin{pmatrix} -\sin\theta_z & \cos\theta_z & 0 \\ -\cos\theta_z & -\sin\theta_z & 0 \\ 0 & 0 & 0 \end{pmatrix}, \quad (10)$$

$$h_k = \Delta t\partial_k\Omega_z = \begin{cases} \Delta t(\gamma G_k + \partial_k\omega) & \text{if} \quad k = r_1, r_2, r_3 \\ \Delta t & \text{if} \quad k = \omega \end{cases} \quad (11)$$

and the initial condition $\partial_k\boldsymbol{M}_0 = 0$. The slope $\partial_k\omega$ of frequency offset is calculated by considering the frequency offset of the voxel and its neighbors in the kth direction.

With Eq. (9) it is possible to calculate PDs of $\boldsymbol{M}$ iteratively. We can think of them as gradients of the components of $\boldsymbol{M}$ with respect to the parameters $\boldsymbol{r}$ and ω. The two terms in brackets on the right-hand side of Eq. (9) can be interpreted as follows: the first increases or decreases intra-voxel gradients in the transverse plane. In the case of spatial coordinates (i.e., $k = r_1, r_2, r_3$), this is due to the presence of external (G_k) or internal ($\partial_k\omega$) field gradients. For $k = \omega$, the component $\partial_\omega\boldsymbol{M}$ (left-hand side of Eq. (9)) is altered if transverse magnetization is present, i.e., it accounts for dephasing and rephasing as a function of time. The second term rotates the magnetization gradients already present according to the offset frequency at each

step. As with the magnetization vector $\boldsymbol{M}$, the magnetization gradients $\partial_k \boldsymbol{M}$ are subject to the same rotation due to RF pulses (R_{RF}) and attenuated by diffusion (A_{D}) and relaxation (E).

A geometrical interpretation of magnetization gradients is given in Fig. 1: for each voxel, $\partial_k \boldsymbol{M}$ indicates the direction and magnitude of change of $\boldsymbol{M}(\boldsymbol{r}, \omega)$ when changing the position along the kth direction, starting from the center of the voxel. Thereby, a useful and reasonable constraint is that the magnetization vector has a the same magnitude everywhere within the voxel, i.e., it is limited to a sphere of radius $|\boldsymbol{M}(0)|$. Thus, we are only interested in the component of $\partial_k \boldsymbol{M}$ perpendicular to $\boldsymbol{M}(0)$, which is given by $(\partial_k \boldsymbol{M})_{\mathrm{perp}} = \partial_k \boldsymbol{M} - (\frac{\boldsymbol{M}}{|\boldsymbol{M}|} \cdot \partial_k \boldsymbol{M}) \frac{\boldsymbol{M}}{|\boldsymbol{M}|}$. It is then possible to extrapolate $\boldsymbol{M}$ for a certain position within the voxel by starting at $\boldsymbol{M}(0)$ (i.e., at the center of the voxel) and traversing on a great circle along the sphere in the direction given by $(\partial_k \boldsymbol{M})_{\mathrm{perp}}$ by an arc length of $s(\boldsymbol{r}, \omega) = |\sum_k k \cdot (\partial_k \boldsymbol{M})_{\mathrm{perp}}|$ (cf. Fig. 1). The tilt angle between $\boldsymbol{M}(\boldsymbol{r}, \omega)$ and $\boldsymbol{M}(0)$ is

$$\alpha(\boldsymbol{r}, \omega) = \frac{s(\boldsymbol{r}, \omega)}{|\boldsymbol{M}(0)|} = \frac{|\sum_k k \cdot (\partial_k \boldsymbol{M})_{\mathrm{perp}}|}{|\boldsymbol{M}(0)|}. \tag{12}$$

2.5. Calculation of MRI signal

In order to account for the effect of intra-voxel magnetization gradients on the acquired MRI signal, the complex signal from a single voxel is calculated by phase-sensitive integration over the voxel. Thereby, the transverse phase in the center of a voxel is given by

$$\phi_0 = \mathrm{atan2}(M_y, M_x). \tag{13}$$

The atan2 function calculates the arc tangent of M_x and M_y with the signs of both arguments used to determine the quadrant of the result (this function is part of the C/C++-programming language). The transverse magnitude is defined by

$$|M_\perp| = \sqrt{M_x^2 + M_y^2}. \tag{14}$$

Linear extrapolation of the phase throughout the voxel yields

$$\phi(\boldsymbol{r}, \omega) = \phi_0 + \boldsymbol{r}\nabla\phi + \omega\partial_\omega\phi \tag{15}$$

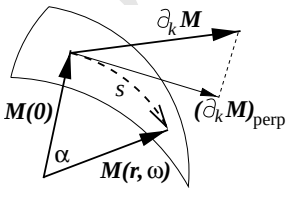

Fig. 1. Geometrical interpretation of magnetization gradients. All magnetization vectors within the voxel lie on a sphere with radius $|\boldsymbol{M}(0)|$. The vector $\boldsymbol{M}(\boldsymbol{r}, \omega)$ can be extrapolated by traversing along the sphere in the direction specified by $(\partial_k \boldsymbol{M})_{\mathrm{perp}}$ and length s. Refer to the text for explanation of symbols.

with PDs of the transverse phase, i.e., of Eq. (13), given by

$$\partial_k \phi = \begin{cases} 0 & \text{if } |M_\perp| = 0, \\ \frac{M_x \partial_k M_y - M_y \partial_k M_x}{|M_\perp|^2} & \text{else.} \end{cases} \tag{16}$$

In the following, it is assumed that $\partial_k |M_\perp| = 0$, i.e. the transverse magnitude does not vary throughout the voxel or with frequency offset. This simplification is reasonable because the primary effect of external fields is to generate a variable phase throughout the voxel.

Integrating over the nth voxel with spatial dimensions L_{r_1}, L_{r_2} and L_{r_3} covering a frequency range L_ω yields the signal

$$S_n = \int_{-\frac{L_{r_1}}{2}}^{\frac{L_{r_1}}{2}} \int_{-\frac{L_{r_2}}{2}}^{\frac{L_{r_2}}{2}} \int_{-\frac{L_{r_3}}{2}}^{\frac{L_{r_3}}{2}} \int_{-\frac{L_\omega}{2}}^{\frac{L_\omega}{2}} |M_\perp| e^{i\phi(\boldsymbol{r}, \omega)} d\omega \, dr_1 \, dr_2 \, dr_3. \tag{17}$$

By applying Fourier integration in each dimension, one obtains

$$S_n = \mathrm{sinc}_{r_1} \mathrm{sinc}_{r_2} \mathrm{sinc}_{r_3} \mathrm{sinc}_\omega |M_\perp| e^{i\phi_0} \tag{18}$$

with

$$\mathrm{sinc}_k = \frac{\sin\left(\frac{L_k}{2}\partial_k\phi\right)}{\frac{L_k}{2}\partial_k\phi}. \tag{19}$$

The overall signal S for each acquisition interval, i.e. the signal received in the RF coil, is then generated by summing over all voxels: $S = \sum_n S_n$.

2.6. Summary of simulation algorithm

To summarize, the following steps are performed in order to simulate an MRI sequence: the array of time intervals is created from the sequence description. For each interval and point of the virtual sample, Eqs. (3) and (9) are used to calculate the magnetization vector $\boldsymbol{M}$ and its intra-voxel gradients $\partial_k \boldsymbol{M}$, respectively. During periods of signal acquisition, Eq. (18) is used to calculate the complex signal, which is transformed to an image by means of standard reconstruction algorithms of ODIN. To derive the algorithm in its closed form presented here, the following assumptions were made:

- To allow an iterative solution of Bloch–Torrey Equations, the hard-pulse approximation was used together with the approximation that relaxations constants are short compared to simulation intervals during RF irradiation. Furthermore, the effect of molecular self diffusion was modelled by continuous damping of the magnetization at each iteration.
- To calculate the tilt angle α of the magnetization vector $\boldsymbol{M}$ within the voxel (Eq. (12)), which will become important in Appendix A to calculate A_{D}, it was assumed that the magnitude of $\boldsymbol{M}$ does not vary throughout the voxel.
- The MR signal (Eq. (17)) is calculated under the approximation that the transverse magnitude is constant within the voxel.

3. Applications

In this section, a number of applications of the algorithm described above are presented together with their results in order to highlight its feasibility for different use cases : the spatial response of single voxels is studied. MAGSI is applied to intra-voxel dephasing around a coaxial cylinder, and echo-planar imaging (EPI) is simulated. The signal of an isochromat distribution is calculated, and finally, the effect of self diffusion is simulated using MAGSI. All simulations were performed on a 3.2 GHz Linux PC. *ST*s were obtained by a timer which was started and stopped right before and after calling the simulation routine in order to avoid bias from program initialization. If appropriate, *ST*s were compared with those of ISUM, whereby ISUM images were simulated by skipping the calculation of magnetization gradients and consequently $\mathrm{sinc}_k = 1$ in Eq. (18).

3.1. Spatial response of MAGSI

Before studying more complex applications of the simulation, the spatial response of single voxels using MAGSI is investigated. Fig. 2 shows a 256×256 simulated image of a 5×5 input matrix with M_0 distributed by a checkerboard pattern using a spoiled gradient-echo (SGE) sequence. Each input voxel extends over several imaging voxels. Because of the very limited number of input voxels, the completion of the simulation took only 8 s.

3.2. Coaxial cylinder model

The well-studied coaxial cylinder model [15] was used to test the feasibility of simulating the effect of field perturbations. The model consists of two coaxial cylinders perpendicular to the main field direction. In our simulations, the outer and inner cylinder had radii of 65 and 4.5 mm and susceptibilities of 9 and 116 ppm, respectively. No signal was obtained from the inner cylinder. The relaxation constants of the outer cylinder were $T_1 = 360$ ms and $T_2 = 320$ ms. An SGE sequence with 128×128 matrix size, 150 mm FOV, $TE = 30$ ms, $TR = 5$ s and 11.1 kHz receiver bandwidth was used. The simulation was performed for a field strength of 1.5 T (equivalent to the setup described in [15]).

In [15], formulae are given to calculate an image of the cylinder model, which was shown to correlate well with actual measurements. Therefore, an image with a large input matrix of 4096×4096 voxels was created using these equations to serve as a reference to estimate the accuracy of simulation results.

Simulated images are shown in Fig. 3. The associated error in the central region with respect to the reference image is depicted in Fig. 4. Using MAGSI, spurious signal in the center is strongly reduced because intra-voxel dephasing is directly accounted for by Eq. (18) with large magnetization gradients (i.e., large $\partial_k \phi$) produced by high $\partial_k \omega$ in central region. The accuracy at all sizes of the input matrix when using MAGSI is comparable to that of the largest size (1024×1024, not shown) of ISUM. Please note, however, that the latter requires an almost impractical *ST* of 14.5 h. Moreover, from Fig. 4 it can be seen that *ST* can be reduced by at least an order of magnitude using MAGSI. In addition, a different slope of the curves in Fig. 4 is observed: the accuracy using ISUM depends strongly on the input-matrix size, whereas with MAGSI, the accuracy is more tolerant with respect to the input size.

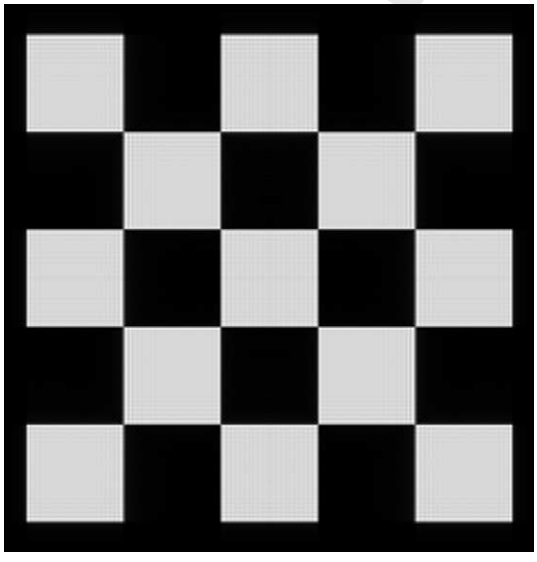

Fig. 2. SGE image (256×256 matrix size, 150 mm FOV) of a 5×5 voxel input matrix with a checkerboard pattern simulated by means of MAGSI.

3.3. EPI simulation

In order to compare the simulation with actual measurements, the brain of a healthy subject was measured on a 3 T Magnetom Trio (Siemens, Erlangen, Germany) with a birdcage head resonator using spin-echo EPI with 64×64 matrix size, 200 mm FOV, 3 mm slice thickness, $TE = 57$ ms and 100 kHz receiver bandwidth. The volume-selective shim was disabled on purpose in order to increase image distortions due to field inhomogeneities. For anatomical reference, images created by a power-reduced variant of the modified driven-equilibrium Fourier transform (MDEFT) sequence [16] were also acquired. The virtual sample was derived from measurements of the same slice during the same session utilizing a Look-Locker sequence for $T_1(\boldsymbol{r})$, a Carr–Purcell–Meiboom–Gill sequence for $T_2(\boldsymbol{r})$ and an SGE sequence with variable *TE* for $\omega(\boldsymbol{r})$ and $M_0(\boldsymbol{r})$. All sequences were programmed using ODIN.

Results of these measurements and simulations are shown in Fig. 5. Image contrast and distortion of the EPI simulations coincide well with those of the actual measurement. Using an 128×128 input matrix, both simula-

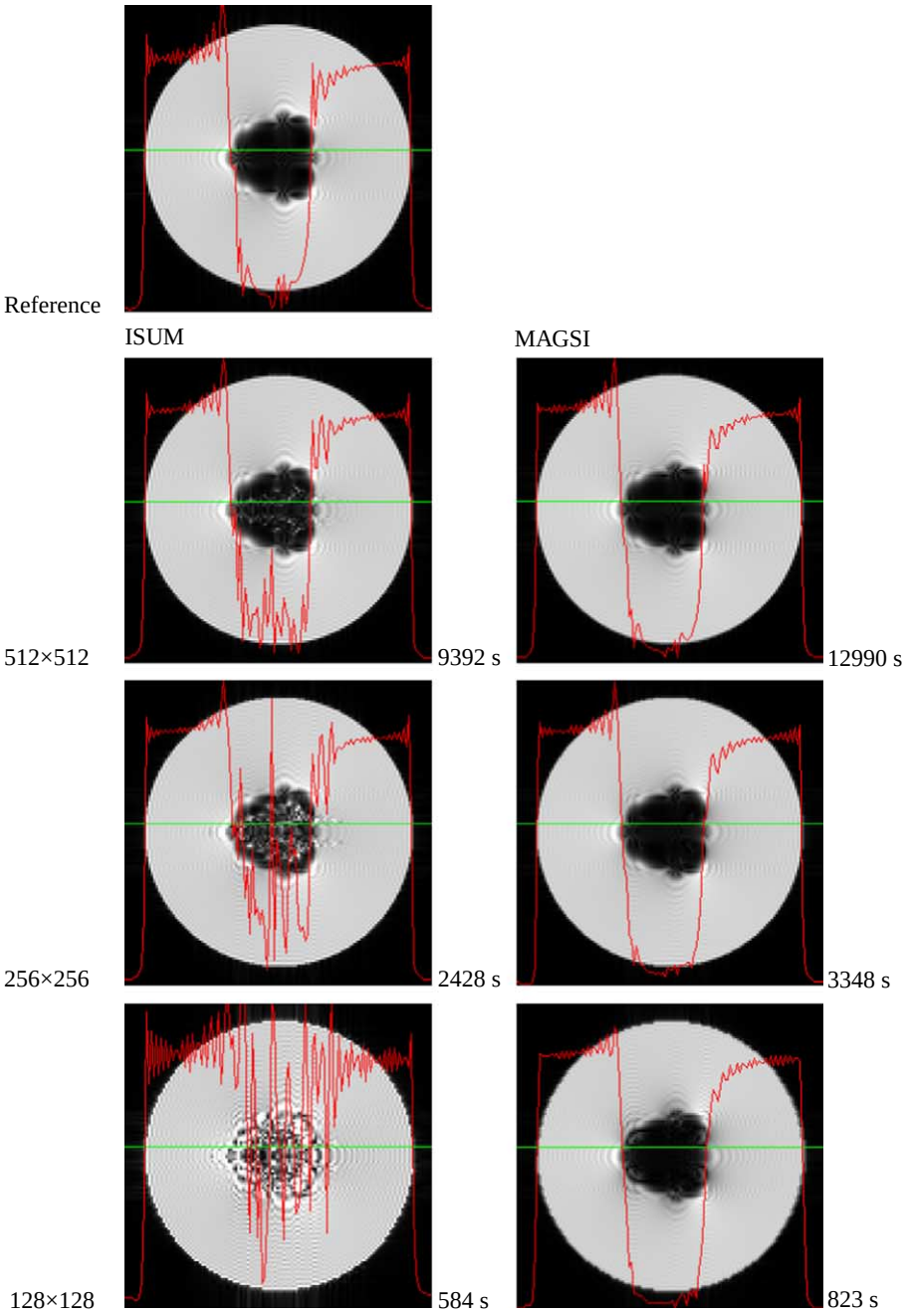

Fig. 3. Simulated images of coaxial cylinder model for different sizes of the input matrix. The top row displays the reference image calculated by formulae given in [15]. Each of the remaining rows was simulated with an input matrix size indicated on the left. The left column displays images obtained by ISUM, and results using MAGSI are shown in the right column. The time required for the simulation is indicated to the right of each image. Red curves show magnitude profiles along the green lines.

tion strategies provide good and almost identical image quality. However, using an input size of 64×64, which is the same as the image size, spurious fluctuations appear when using ISUM. In contrast, the use of MAGSI results in a smooth image, which is equivalent to that of a larger input size. The images simulated with an 32×32 input matrix demonstrate what happens if input voxels are larger than imaging voxels: with ISUM single isochromats become visible, and MAGSI provides images which are smoothed heavily.

By comparing the *ST*s of images with smallest input size but without visible artifacts (128×128 for ISUM and 64×64 for MAGSI), it can be roughly estimated that MAGSI provides a four-fold increase in simulation speed without sacrificing accuracy. Thereby, it is important to note that *ST*s do not scale linearly with the number of input voxels, as expected (for instance: $4 \times 14.2\ \text{s} \neq 99.9\ \text{s}$, see Fig. 5, ISUM with 64×64 and 128×128). The abberation is probably caused by memory caching within the computers processor, causing overhead for applications

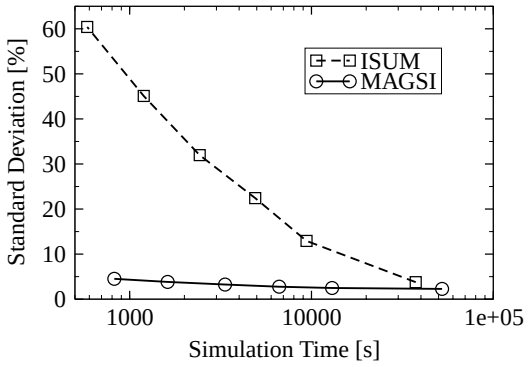

Fig. 4. Difference between the reference image and the simulated images of the coaxial cylinder model in a central region (disk with radius 25 mm) as a function of *ST*. Standard deviation is taken relative to the maximum intensity in the outside region. The size of the input matrix for each point indicated by symbols from left to right was $N \times N$ with $N = 128$, 181, 256, 362, 512, and 1024. Please note the logarithmic scale of the abscissa.

which exceed its limit. This interpretation is supported by the fact that for smaller input sizes, i.e., if the cache size is sufficient to accommodate the whole magnetization during simulation, *ST* is approximately linear in the number of input voxels. However, as the simulation presented here is a realistic application, it is admissible to take this overhead into account when comparing *ST*s.

3.4. Frequency distribution

In the previous examples, MAGSI has been used to interpolate the magnetization between spatial positions ($k = x, y, z$). It may also be used to interpolate between frequency offsets ($k = \omega$) in order to reduce the number of isochromats. To test this, the free-induction decay (FID) of a Gaussian-shaped frequency distribution with full-width-at-half-maximum (FWHM) of 4.77 Hz, $T_2 = 200$ ms and an isochromat separation of 2.5 Hz (8 isochromats) after a $\pi/2$ pulse at $t = 0$ (comparable to Fig. 3b in [9]) is shown in Fig. 6. It is clear that the use of MAGSI provides an FID in which spurious refocusing, which leads to artificial signal maxima, is reduced significantly. However, if the accuracy is analyzed as a function of *ST* (Fig. 7), the performance of MAGSI is slightly worse than that of ISUM.

3.5. Diffusion weighting with a stimulated echo

The PDs of $\boldsymbol{M}$ can also be used to simulate the effect of self-diffusion by calculating Eqs. (3) and (5) by means of formulae for β_1 and β_2 given in Appendix A. The simulation of a diffusion-weighted spin-echo sequence, which is commonly applied for this purpose, is trivial because only transverse magnetization plays a role, i.e., only β_2 has to be known, which is given by the Stejskal–Tanner formula. Therefore, as a more sophisticated example, a stimulated-echo sequence (3 hard-$\pi/2$ pulses) was simulated with $TE = 28$ ms, a mixing time of 50 ms and two gradient pulses enclosing the sequence of identical RF pulses. The gradient amplitude was adjusted to yield *b*-values in the range 100–2000 s/mm^2. An off-resonance frequency distribution with FWHM of 100 Hz and a uniform diffusion coefficient of 10^{-3} mm^2/s was used as input for simulation. The simulated spectra are depicted side-by-side in Fig. 8. There is good agreement between the specified diffusion coefficient and the result of the fit: the error is less than 1%.

4. Discussion

The algorithm presented here allows a straightforward implementation. It is now an integral part of ODIN which means that its source code is freely available and a large number of sequences, which were validated by actual measurements, can be simulated.

The application to the coaxial cylinder model shows that by using ISUM to simulate the effect of field perturbations, at least 8 isochromats per direction are necessary to reduce the error in the reconstructed image to a few percent (cf. Fig. 4). This exceeds previous estimations of three isochromats per direction [7]. This discrepancy is caused by the difficulty to simulate signal attenuation due to field-inhomogeneity-induced intra-voxel dephasing accurately with a limited number of isochromats because spurious rephasing can occur. However, by using MAGSI (linear) intra-voxel dephasing is modeled correctly and the error, and hence the *ST*, can be reduced enormously.

The simulation results of Fig. 3 show more abberations between ISUM and MAGSI than those in Fig. 5. This is due to the fact that the image patterns of Fig. 3 are dominated by intra-voxel dephasing which is handled more efficiently by MAGSI than by ISUM. On the other hand, the contrast in Fig. 5 is dominated by differences in T_2 which is simulated equally in ISUM and MAGSI.

Calculating the magnetization gradients in addition to the magnetization vector in the MAGSI technique increased *ST* by approximately 30–100% in the imaging simulations depending on the sequence used. One would expect a larger overhead because the number of computational steps required to calculate Eq. (9) is considerably higher than that required for Eq. (3), and in addition, Eq. (18) has to be calculated. However, the computationally expensive trigonometric and exponential functions of E, $\mathrm{R_{RF}}$, $\partial_k \mathrm{R}_z$, and R_z in Eq. (9) have already been calculated for the magnetization vector and can be reused during one iteration. Another great advantage is that Eq. (18) has to be evaluated only during signal acquisition, i.e., only during a fraction of the whole sequence simulation. This overhead is negligible because the size of the input matrix can be reduced significantly by using MAGSI in comparison to ISUM (especially if field perturbations are involved). In addition, it becomes more robust and fault-tolerant as the dependency on the size of the input matrix is greatly reduced.

By using an input-matrix size which is smaller than the desired image size, the spatial response to a particular input voxel extends over several imaging voxels. An extreme example is Fig. 2. In cases where simple objects like this

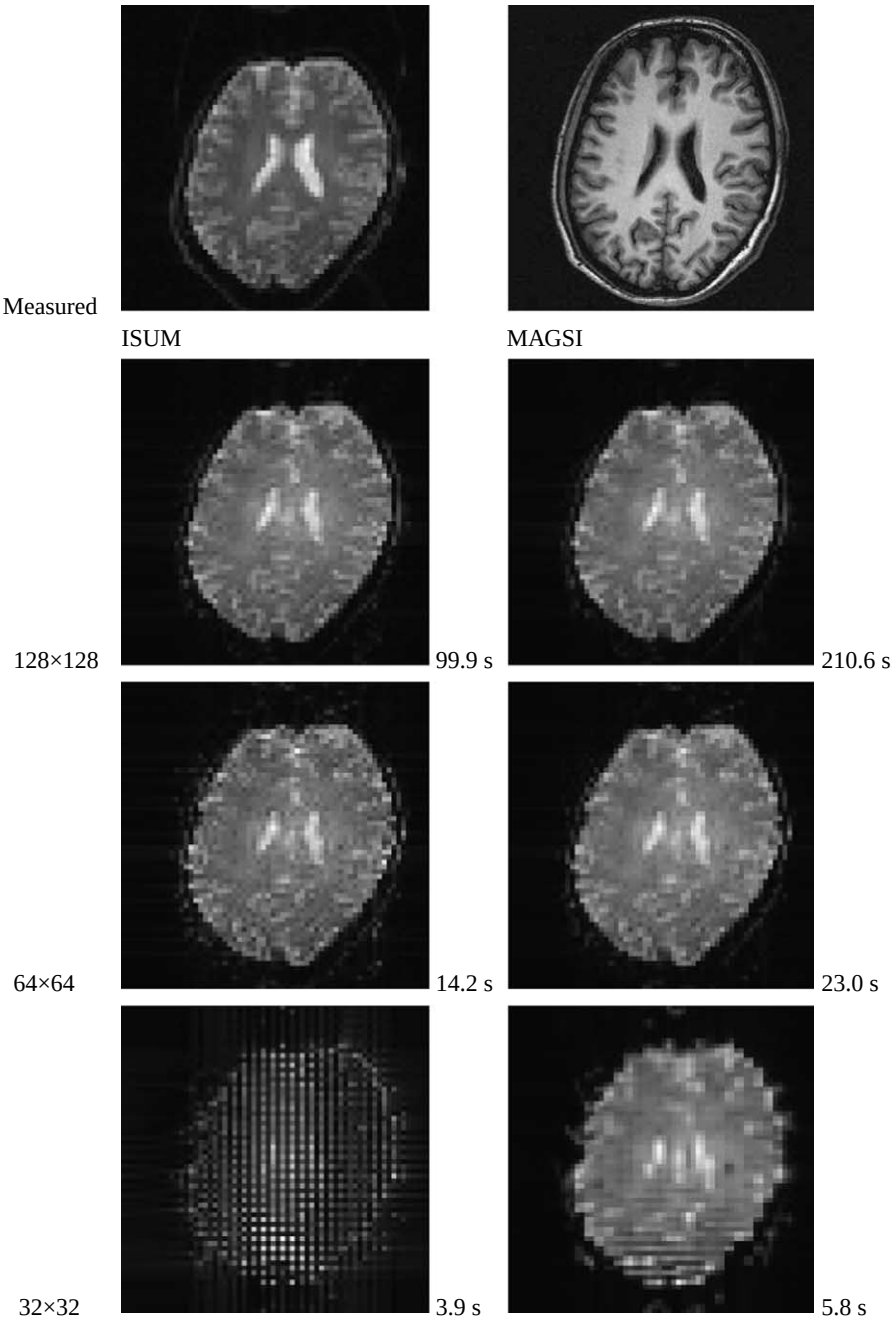

Fig. 5. Images of human brain. The top row depicts the EPI (left) and MDEFT (right) measurement. The rest of the layout is equivalent to that of Fig. 3.

checkerboard are sufficient to test the quality of MRI sequences, *ST* is negligible. Thus, the simulation can become an integral part of sequence development process without the need of time-consuming measurements.

In addition to spatial interpolation, MAGSI can also be used to increase the accuracy of simulating the signal from frequency distributions by interpolating between isochromats, as demonstrated by the simulation of FID. However, in the example presented, it did not increase the efficiency in terms of *ST*. This is because the sequence used is dominated by periods of signal acquisition which are costly for MAGSI: Eq. (18) has to be calculated at each iteration. On the other hand, MAGSI does not worsen the simulation efficiency. It can be expected that it will become more useful for complicated sequences with many RF pulses and gradients.

It should be noted that in [2,10], intra-voxel dephasing is accounted for by shortening the transverse magnetization according to the *current* field gradients in the voxel during each sample time. This accumulative damping of the signal models continuous dephasing correctly, but cannot account for rephasing (e.g., a gradient echo cannot be generated from a single voxel) as it does only keep track of the magnitude of the magnetization vector. Thus, intra-voxel *rephasing* can only be achieved by the accumulative effect of many isochromats. In contrast, the approach presented

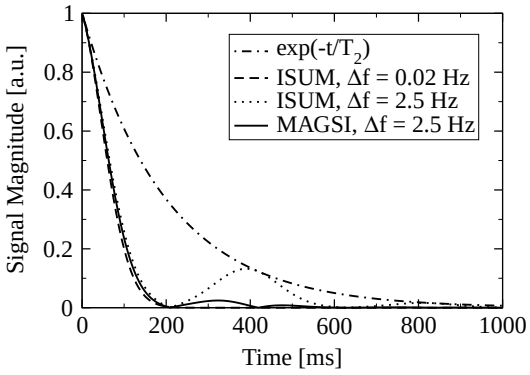

Fig. 6. Simulated FID of a Gaussian isochromat distribution. The exponential T_2 decay and the ISUM timecourse with $\Delta f = 0.02$ Hz serve as a reference as they are the limiting cases of a single and a very large number of isochromats, respectively. The simulations with $\Delta f = 2.5$ Hz depict the effect of insufficient frequency spacing on the signal obtained by ISUM and MAGSI.

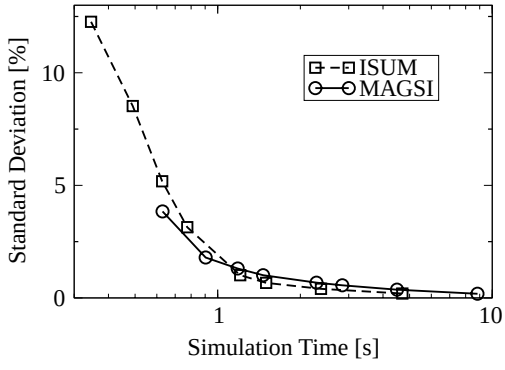

Fig. 7. Difference between simulated free-induction decay and reference timecourse with $\Delta f = 0.02$ Hz (cf. Fig. 6) as a function of ST. For both techniques, ISUM and MAGSI, isochromat separations of $\Delta f = 4.8$, 3.2, 2.5, 1.9, 1.2, 0.96, 0.60, and 0.30 Hz were used (symbols from left to right). Standard deviation is taken relative to the maximum magnitude.

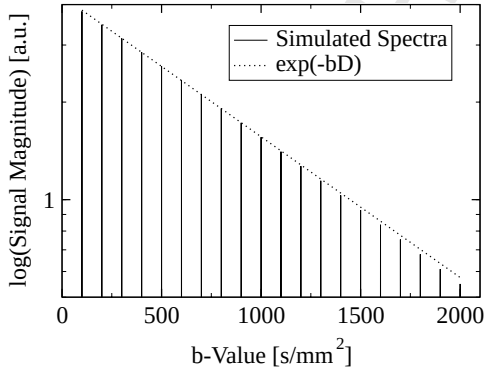

Fig. 8. Logarithmic magnitude of spectra for 20 different b-values aligned side-by-side together with the expected signal attenuation as a function of b-value (dotted line). An exponential fit of the peak magnitude vs. b-value yields a diffusion coefficient of 1.007×10^{-3} mm^2/s.

here treats rephasing and dephasing equally by keeping track of the magnetization gradients.

In addition to modeling intra-voxel dephasing, the PDs of magnetization can also be used to calculate the signal attenuation due to molecular self-diffusion. The formulae presented in Appendix A provide a general framework to calculate the attenuation iteratively. Thus, it can be applied to any MR sequence. The simulation of the diffusion-weighted stimulated-echo sequence yielded excellent agreement between simulation and theoretical prediction of the Stejskal–Tanner formula. However, it remains to be proven that this corresponds with measurements, and that the framework is also applicable to more complex sequences, e.g. those based on steady-state free precession.

In order to increase the accuracy of simulation, it would be possible to trace not only the magnetization gradients, i.e. the first order PDs, but also higher order PDs. These could be obtained by calculating again PDs of Eq. (9). However, it is questionable whether this would also increase efficiency of the simulation by reducing ST because the primary effect of external and internal gradients is to establish a linear dependency which is properly covered by first-order PDs.

There is a close relation between spatial PDs of the transverse phase ($\partial_k \phi$ with $k = x, y, z$) and k-space coordinates. For example, both are identical when studying dephasing due to the application of gradients after a single excitation without field perturbations (Eq. (11) with $\partial_k \omega = 0$). However, the difference is that k-space analysis requires a priori knowledge about the intention of RF pulses, e.g., whether they are used for excitation or refocusing, in order to trace the k-space trajectory of a certain coherence pathway. In contrast, this is automatically taken into account by MAGSI. For instance, a π-refocusing pulse will reflect magnetization gradients in the transverse plane (Eq. (9) with $R_{RF} = \mathrm{diag}(1, -1, -1)$) which is equivalent to reflecting k-space coordinates.

5. Conclusions

The MAGSI algorithm has been introduced which increases efficiency when simulating Bloch–Torrey equations. That is, it increases simulation accuracy without elongating simulation time, or alternatively, decreases simulation time while retaining accuracy. It has been shown that MAGSI is most applicable to (linear) intra-voxel dephasing due to field perturbations. In the specific case of the cylinder model, simulation time was reduced by at least an order of magnitude compared to conventional summation techniques. Although to a lesser extent, MAGSI is also useful to increase simulation efficiency of typical imaging sequences by reducing artifacts due to the discrete nature of the input matrix. Another result of the algorithm is that the effect of molecular self-diffusion on the MR signal can be calculated iteratively.

Acknowledgments

The authors thank Chunlei Liu for his excellent comments during preparation of the manuscript.

Appendix A

In order to calculate β_1 and β_2 using Eq. (1), we first need to derive a relation for $\nabla^2 \boldsymbol{M}_i$, i.e., for ∇^2 acting on $\boldsymbol{M}$ at a fixed point in time at the end of an simulation interval with index i. Because it is assumed that $\boldsymbol{M}_i$ is limited to a sphere of radius $|\boldsymbol{M}_i|$ within the voxel and that higher-order PDs can be neglected, $\boldsymbol{M}_i(\boldsymbol{r})$ will be some linear combination of trigonometric functions with an argument α given by Eq. (12). Partial derivation then yields

$$\nabla^2 \boldsymbol{M}_i = -(\nabla\alpha)^2 \boldsymbol{M}_i = -d\boldsymbol{M}_i \tag{20}$$

with

$$d = \frac{\sum_{l=1}^{3} (\partial_{r_l} \boldsymbol{M}_i)^2}{\boldsymbol{M}_i^2}. \tag{21}$$

The evolution of the complex transverse magnetization $M_\perp = M_x + \mathrm{i}M_y$ during periods of free precession with constant (internal and/or external) gradient $\nabla\Omega_z$ and free isotropic diffusion with coefficient D (and neglecting relaxation) is described by the first two rows of Eq. (1)

$$\dot{M}_\perp = -\mathrm{i}M_\perp \boldsymbol{r}\nabla\Omega_z + D\nabla^2 M_\perp. \tag{22}$$

We will use the approach

$$M_\perp(\boldsymbol{r}, t) = \exp[-\beta_2(t)D - \mathrm{i}t\boldsymbol{r}\nabla\Omega_z] M^i_\perp(\boldsymbol{r}) \tag{23}$$

in order to calculate $\beta_2(t)$ with $\beta_2(0) = 0$. Please note that this differs from the approach used in [12] by $M^i_\perp(\boldsymbol{r})$, which is an additional initial dependency of $M_\perp$ upon $\boldsymbol{r}$ at $t = 0$, i.e., at the end of the previous ith iteration. This generalization is necessary for proper step-wise simulation of diffusion.

Substituting Eq. (23) in Eq. (22) and using Eq. (20), one obtains

$$\dot{\beta}_2 = (t\nabla\Omega_z)^2 - 2t(\nabla\Omega_z)(\nabla\phi_i) + d + 2it\frac{\nabla|M^i_\perp|}{|M^i_\perp|}\nabla\Omega_z \tag{24}$$

with $\nabla\phi_i$ given by Eq. (16). As with calculation of MR signal, it is assumed that $\nabla|M^i_\perp| = 0$ so that the last term can be neglected. Integration of Eq. (24) then yields

$$\beta_2 = \Delta t\left[\frac{1}{3}\boldsymbol{h}^2 - \boldsymbol{h}\nabla\phi_i + d\right] \tag{25}$$

with $\boldsymbol{h} = \Delta t\nabla\Omega_z$ of Eq. (11). It can be verified that this iterative equation produces the correct Stejskal–Tanner formula [17].

The above strategy incorporates the effect of diffusion on the transverse magnetization only. For a comprehensive simulation, it is also necessary to calculate the attenuation of longitudinal magnetization due to diffusion. For instance, to simulate diffusion weighting with a stimulated echo, where magnetization is stored in longitudinal direction between two RF pulses, the effect of diffusion during this period must also be considered. Hence, we take the third component of Eq. (1) and neglect T_1 relaxation:

$$\dot{M}_z = D\nabla^2 M_z. \tag{26}$$

In analogy to Eq. (23), the approach

$$M_z(\boldsymbol{r}, t) = \exp[-\beta_1(t)D] M^i_z(\boldsymbol{r}) \tag{27}$$

is used to solve for β_1. The initial condition M^i_z is given by M_z at the end of the previous iteration. Substituting Eq. (27) into Eq. (26), using Eq. (20) and integrating β_1, one obtains

$$\beta_1 = d\Delta t. \tag{28}$$

References

[1] J. Bittoun, J. Taquin, M. Sauzade, A computer algorithm for the simulation of any nuclear magnetic resonance (NMR) imaging method, Magn. Reson. Imaging 2 (1984) 113–120.
[2] M.B.E. Olsson, R. Wirestam, B.R.R. Persson, A computer simulation program for MR imaging: application to RF and static magnetic field imperfections, Magn. Reson. Med. 34 (1995) 612–617.
[3] I. Marshall, Simulation of in-plane flow imaging, Conc. Magn. Reson. Part A 11 (1999) 379–392.
[4] R. Trampel, T.H. Jochimsen, T. Mildner, D.G. Norris, H.E. Möller, Efficiency of flow-driven adiabatic spin inversion under realistic experimental conditions: a computer simulation, Magn. Reson. Med. 51 (2004) 1187–1193.
[5] T.H. Jochimsen, M. von Mengershausen, ODIN - object-oriented development interface for NMR, J. Magn. Reson. 170 (2004) 67–78, http://od1n.sourceforge.net.
[6] R.M. Summers, L. Axel, S. Israel, A computer simulation of nuclear magnetic resonance imaging, Magn. Reson. Med. 3 (1986) 363–376.
[7] P. Shkarin, R.G.S. Spencer, Time domain simulation of Fourier imaging by summation of isochromats, J. Imaging Syst. Technol. 8 (1997) 419–426.
[8] A.R. Brenner, J. Kürsch, T.G. Noll, Parallelized high-performance MRI simulation on a workstation cluster, ISMRM 3 (1997) 2052.
[9] R.K.-S. Kwan, A.C. Evans, G.B. Pike, MRI simulation-based evaluation of image-processing and classification methods, IEEE Trans. Med. Imaging 18 (1999) 1085–1097.
[10] D.A. Yoder, Y. Zhao, C.B. Paschal, J.M. Fitzpatrick, MRI simulator with object-specific field map calculations, Magn. Reson. Imaging 22 (2004) 315–328.
[11] H. Benoit-Cattin, G. Collewet, B. Belaroussi, H. Saint-Jalmes, C. Odet, The SIMRI project: a versatile and interactive MRI simulator, J. Magn. Reson. 173 (2005) 97–115.
[12] H.C. Torrey, Bloch equations with diffusion terms, Phys. Rev. 104 (1956) 563–565.
[13] H.C. Torrey, Transient nutation in nuclear magnetic resonance, Phys. Rev. 76 (8) (1949) 1059–1068.
[14] M. Shinnar, S. Eleff, H. Subramanian, J.S. Leigh, The synthesis of pulse sequences yielding arbitrary magnetization vectors, Magn. Reson. Med. 12 (1989) 74–80.
[15] C.J.G. Bakker, R. Bhagwandien, M.A. Moerland, M. Fuderer, Susceptibility artifacts in 2DFT spin-echo and gradient-echo imaging: the cylinder model revisited, Magn. Reson. Imaging 11 (1993) 539–548.
[16] D.G. Norris, Reduced power multislice MDEFT imaging, J. Magn. Reson. Imaging 11 (2000) 445–451.
[17] E.O. Stejskal, J.E. Tanner, Spin diffusion measurements: spin echoes in the presence of a time-dependent field gradient, J. Chem. Phys. 42 (1965) 288–292.